ADVANCED HEALTHCARE MATERIALS
www.advhealthmat.de

Engineered Cell-Derived Vesicles Displaying Targeting Peptide and Functionalized with Nanocarriers for Therapeutic microRNA Delivery to Triple-Negative Breast Cancer in Mice

*Rajendran JC Bose, Uday Sukumar Kumar, Fernando Garcia-Marques, Yitian Zeng, Frezghi Habte, Jason R McCarthy, Sharon Pitteri, Tarik F Massoud, and Ramasamy Paulmurugan**

Polymeric nanocarriers (PNCs) can be used to deliver therapeutic microRNAs (miRNAs) to solid cancers. However, the ability of these nanocarriers to specifically target tumors remains a challenge. Alternatively, extracellular vesicles (EVs) derived from tumor cells show homotypic affinity to parent cells, but loading sufficient amounts of miRNAs into EVs is difficult. Here, it is investigated whether uPAR-targeted delivery of nanococktails containing PNCs loaded with therapeutic antimiRNAs, and coated with uPA engineered extracellular vesicles (uPA-eEVs) can elicit synergistic antitumor responses. The uPA-eEVs coating on PNCs increases natural tumor targeting affinities, thereby enhancing the antitumor activity of antimiRNA nanococktails. The systemic administration of uPA-eEV-PNCs nanococktail shows a robust tumor tropism, which significantly enhances the combinational antitumor effects of antimiRNA-21 and antimiRNA-10b, and leads to significant tumor regression and extension of progression free survival for syngeneic 4T1 tumor-bearing mice. In addition, the uPA-eEV-PNCs-antimiRNAs nanococktail plus low dose doxorubicin results in a synergistic antitumor effect as evidenced by inhibition of tumor growth, reduction of lung metastases, and extension of survival of 4T1 tumor-bearing mice. The targeted combinational nanococktail strategy could be readily translated to the clinical setting by using autologous cancer cells that have flexibility for ex vivo expansion and genetic engineering.

1. Introduction

Breast cancer (BC) has now overtaken lung cancer as the world's most diagnosed cancer and is a leading cause of cancer-related deaths in women worldwide.[1] BCs that are immunohistochemically characterized by the lack of estrogen receptor (ER), progesterone receptor (PR), and human epidermal growth factor receptor 2 (HER2) are classified as triple-negative breast cancer (TNBC), which account for ≈20% of all BCs.[2] The overall survival rate of TNBC patients diagnosed with metastatic disease is ≈13 months and is still significantly lower than that of non-TNBC patients across any stage at diagnosis, which embodies an important therapeutic challenge.[3]

BC cell-derived vesicles (BCCDVs) are heterogeneous sub-micron-sized proteolipid vesicles formed by direct plasma membrane budding from cancer cells. These vesicles carry a diverse group of tumor-associated adhesive proteins, antigens, and loaded cellular macromolecules.[4] BCCDVs

R. J. Bose, U. S. Kumar, F. Garcia-Marques, F. Habte, T. F Massoud, R. Paulmurugan
Molecular Imaging Program at Stanford (MIPS)
and Bio-X Program
Department of Radiology
School of Medicine
Stanford University
Stanford, CA 94305–5427, USA
E-mail: paulmur8@stanford.edu

The ORCID identification number(s) for the author(s) of this article can be found under https://doi.org/10.1002/adhm.202101387

R. J. Bose, U. S. Kumar, F. Habte, S. Pitteri, R. Paulmurugan
Canary Center at Stanford for Cancer Early Detection
Department of Radiology
School of Medicine
Stanford University
Stanford, CA 94305–5427, USA

Y. Zeng
Department of Materials Science and Engineering
Stanford University
Stanford, CA 94305-4034, USA

J. R McCarthy
Biomedical and Translational Medicine
Masonic Medical Research Institute
Utica, NY 13501, USA

Dedicated to the memory of Dr. Sanjiv Sam Gambhir

DOI: 10.1002/adhm.202101387

and their cell adhesion molecules (CAMs) have pivotal roles in TNBC metastasis owing to their homotypic cancer-targeting mechanisms.[5] Likewise, BCCDVs possess inherent advantages compared to synthetic liposomes, including superior cargo loading ability, long life span in the circulation, rapid and higher cell internalization, and the capacity to cross biological and intratumoral barriers, making them highly suitable for therapeutic cargo deliveries during TNBC therapy.[5,6] Despite to-date testing in human clinical trials, BCCDV-based therapies have not been approved for clinical applications.[7] This is in part owing to the inability to rationally formulate BCCDVs with therapeutic cargos with potent and reproducible therapeutic activity. To overcome this problem, a range of bioengineering strategies have been developed.[8] Among them, the use of bioengineered BCCDVs using BCs engineered to display targeting peptide sequences is one efficient approach to enhance the functionality of BCCDVs.[9] Specifically, peptides are excellent candidates for engineering cancer cells to isolate cancer cell-derived vesicles (CCDVs) and surface molecules with little change in immunogenicity. Furthermore, the simple structures of peptides, the easy process to engineer them, and low synthesis costs, make them useful agents in targeted delivery approaches in cancer therapy.[10,11] With the discovery of many targeting peptides homing to cancers through phage display and in vivo biopanning technologies, there are plenty of opportunities to explore the potential of engineered CCDVs for targeted TNBC therapy.[10] Appreciation of biological roles and material properties of CCDVs has facilitated cancer therapy, as has engineering CCDVs with targeting peptides to improve the specificity of CCDVs in recognizing cancer cells through receptor-ligand binding.[9] In CCDV biogenesis, transmembrane proteins such as lactadherin, lysosome-associated membrane protein-2B (LAMP-2b), and platelet-derived growth factor receptor (PDGFR) are enriched in the CCDVs compartment and provide opportunities to genetically engineer these proteins to display selective targeting peptides on their surfaces.[12] This process confers CCDV targeting capability to BC cells bearing cognate receptors including androgen receptor, epidermal growth factor receptor (EGFR), fibroblast growth factor receptor (FGFR), vascular endothelial growth factor receptor (VEGFR), and urokinase plasminogen activator receptor (uPAR).[11,13] Among these, uPAR plays a critical role in cell growth, motility, invasiveness, and the level of uPAR expression has been often associated with poor prognosis in TNBC patients.[14,15] Furthermore, uPAR expression is positively correlated with a stage of advanced disease and drug-resistant phenotype.[15,16] Previously, we and others have developed urokinase-type plasminogen activator (uPA) -mediated uPAR targeted nanoparticles (NPs) for cancer therapy using MDA-MB-231 TNBC animal tumor models.[17,18]

MicroRNAs (miRNAs) are small, non-coding, endogenous molecules that are involved in post-translational regulation of gene expression in multicellular organisms.[17,19] In TNBC, dysregulation of miRNAs has been associated with a broad spectrum of cellular processes. We and others have found that miRNA-10b and miRNA-21 are overexpressed in TNBCs, and this correlates with chemoresistance and metastatic potential.[17,19,20] Simultaneously antagonizing multiple endogenous miRNAs could affect target mRNAs of different genes and result in an additive or enhanced therapeutic effect.[21] However, the lack of safe and efficient approaches to deliver miRNAs in a targeted manner to TNBCs in vivo hinders clinical translation of miRNA modulation therapy.[21] Intravenously injected miRNAs can be rapidly degraded by nucleases and therefore need to be protected to extend their circulation lifetime in the blood to achieve an efficient therapeutic effect.[21] Encapsulation of miRNAs within biodegradable polymeric nanocarriers can provide sufficient protection from nucleases and improve the sustained release of miRNAs for long periods to enhance the therapeutic efficacy of miRNAs. We have shown the production and preclinical validation of miRNA-loaded PLGA-NPs in rodent,[22] pig,[23] and dog[24] models. We established diverse strategies to enhance the overall therapeutic efficacy of miRNAs in vivo.[25] Among the various strategies, CCDV-mediated homotypic tumor targeting has shown promising results in a TNBC tumor-bearing nude mouse model.[26]

2. Results and Discussion

Here, we employed a bioengineering approach to enhance the targeting function of NCs by surface coating with extracellular vesicles (EVs) derived from 4T1-TNBC cells, and thereby enhancing the delivery and the overall therapeutic efficacy of antisense miRNAs. We also tested this targeted nanococktail approach using uPA peptide bioengineered 4T1-derived EV-functionalized miRNA nanoformulations as a potential strategy to treat TNBC. We engineered 4T1 cancer cells to display uPAR targeting uPA or negative control scrambled-uPA (Sc-uPA) peptide as a fusion protein with PDGFR. We used 4T1-engineered(e)EVs isolated from these cells to functionalize PLGA nanocarriers pre-loaded with either antisense-miRNA-21 (antimiRNA-21) or antisense-miRNA-10b (antimiRNA-10b) with the encapsulation efficiency of 70 ± 5%, collectively dubbed as "eEV-Polymeric Nanocarriers (eEV-PNCs)" (**Figure 1**, Figure S1, and Table S1, Supporting Information). The preparation of 4T1-eEV-PNCs requires two steps: in the first, we prepared genetically engineered 4T1-eEVs that display uPAR targeting uPA or control Sc-uPA. We transfected the constructs expressing the genes coding for the C-terminal transmembrane domain of PDGFR with uPA or Sc-uPA as a fusion protein (**Figure 2**a) into 4T1 cells, and we selected the clones stably expressing the genes with 200 ng mL^{-1} of puromycin. After the positive selection, we purified the Sc-uPA and uPAR targeting uPA peptides displaying 4T1-eEVs using a standard ultracentrifugation method, which we optimized in the lab previously[26] (Figure S1, Supporting Information). Dynamic Light Scattering (DLS) revealed that the isolated eEVs were in the nanometer size range (200–300 nm), with an average size of ≈250 nm and an average concentration of 1.91e8 ± 7.5 e6 particles mL^{-1} of conditioned media (Figure 2b). Electron microscopy revealed heterogeneous size and shape of eEVs, with unilamellar and multilamellar phospholipid layered membrane structures (Figure 2c); the size was consistent with the size range previously reported for typical 4T1-EVs.[27] The DLS analysis further confirmed the size of eEV-Sc-uPA and eEVs-uPA as 247 ± 16.6 and 253 ± 23 nm, respectively (Table S1, Supporting Information). Furthermore, the DLS analysis revealed that the size and charge of non-engineered and engineered 4T1 (Sc-uPA and uPA) cell-derived EVs were not significantly different (Figure S2, Supporting Information), highlighting that the bioengineering process did not

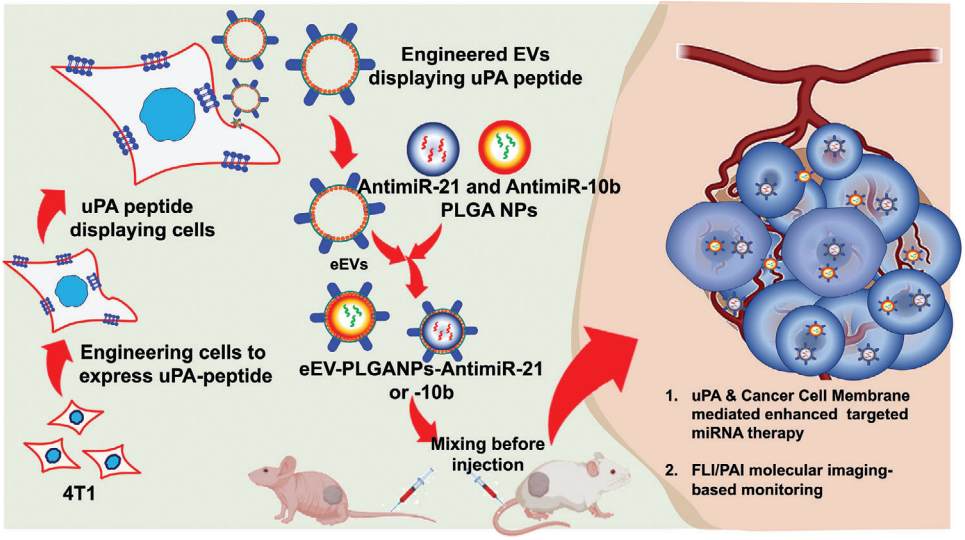

Figure 1. Schematic illustration strategy of 4T1-engineered extracellular vesicles (eEVs) that display uPAR targeting uPA or scrambled uPA (Sc-uPA) peptide-functionalized PLGA-nanocarriers separately loaded with antimiRNA-21 or antimiRNA-10b.

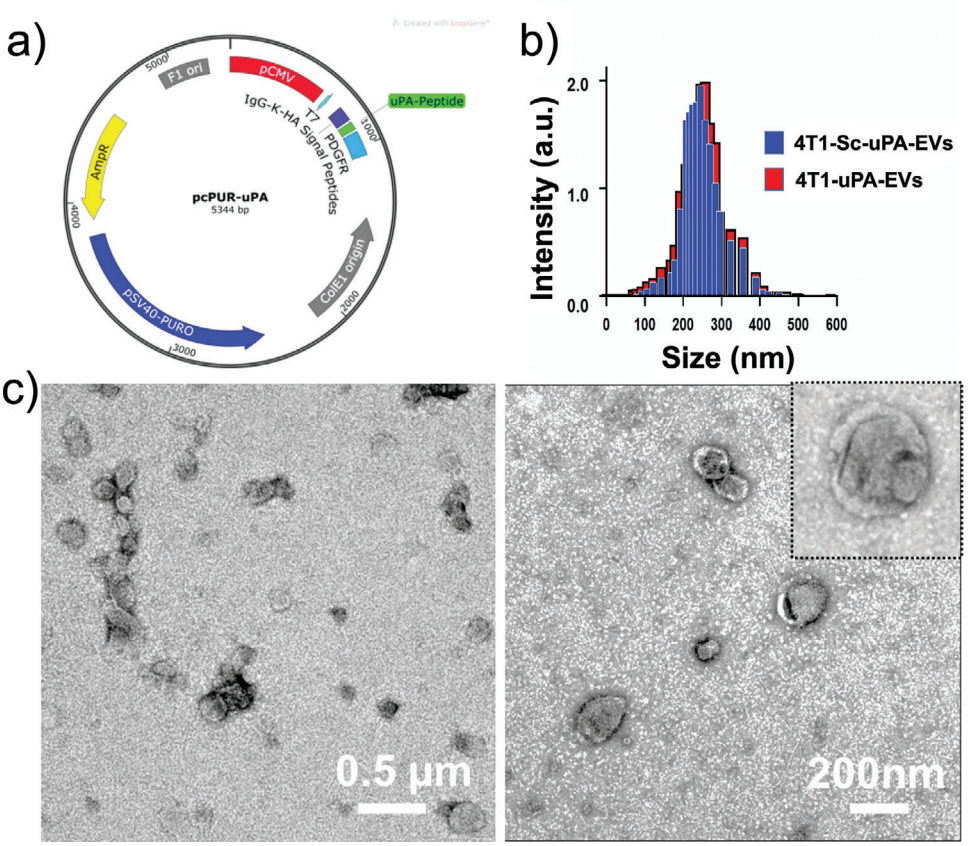

Figure 2. a) Schematic illustration shows the pcPUR-uPA vector map with PDGFR transmembrane domain fused uPA or negative control scrambled-uPA (Sc-uPA) insert sequence used to engineer the 4T1 cancer cells to display uPAR targeting uPA or Sc-uPA peptide as a C-terminal fusion protein with PDGFR. b) DLS revealing comparative size distribution of 4T1-eEVs isolated from cells engineered to display uPA and Sc-uPA ($n = 3$). c) TEM image of eEVs isolated from 4T1 cancer cells engineered to express uPA peptide ($n = 3$). Insert figure within image (c) shows the spherical shaped proteo-lipid vesicles of eEVs isolated from 4T1 cancer cells engineered to express uPA peptide at higher magnification.

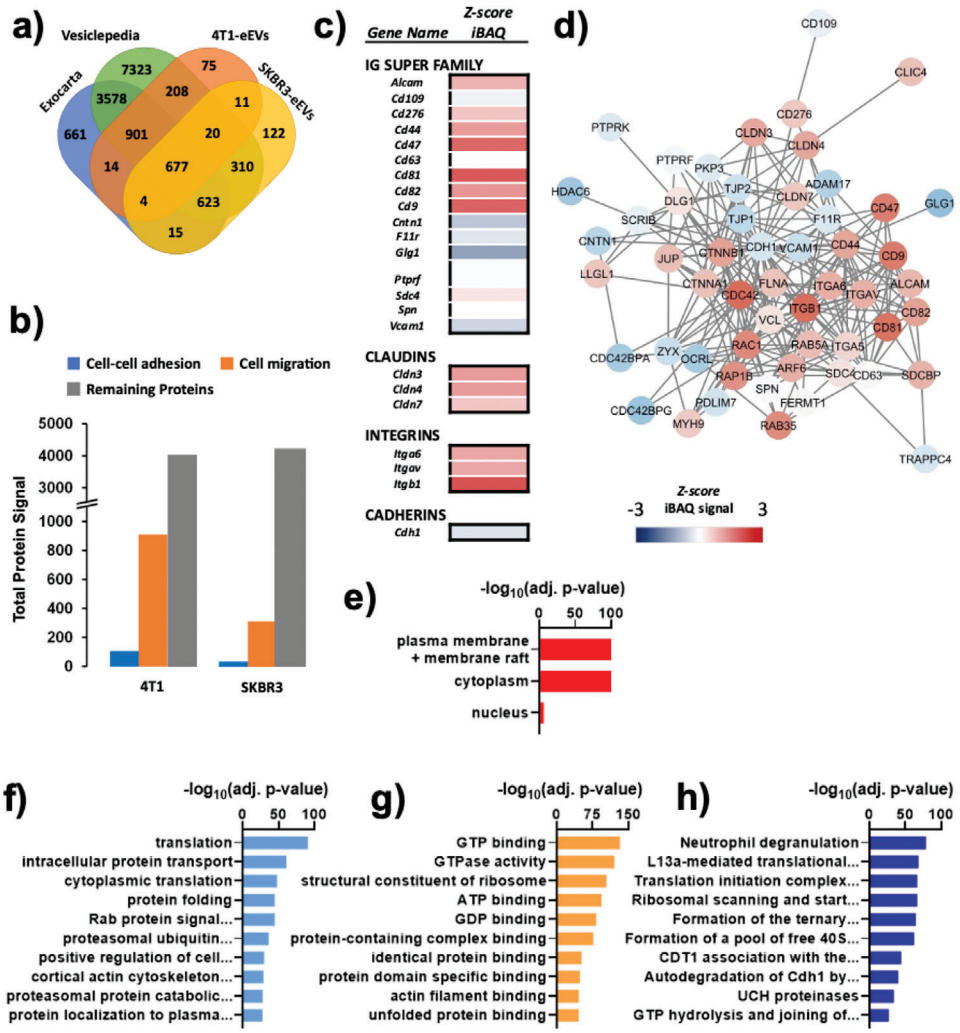

Figure 3. Proteomic analysis of 4T1-eEVs. a) Venn diagram shows the comparison of protein identifications (4T1 and SKBR3) found in our study and reported by Vesiclepedia and ExoCarta. b) Total protein signal from 41T-eEVs and SKBR3-eEVs by category. c,d) Abundant cancer cell adhesion proteins identified in 4T1-eEVs. Z-score iBAQ quantification values are shown by color. Gene ontology (GO) analysis of identified proteins from 4T1-eEVs sample. Gene enrichment was performed by e) GO cellular component, f) GO biological process, g) molecular function, and h) reactome pathway analysis. Protein enrichment is represented as −log10 of *p*-value after Bonferroni correction.

change the size and charge of 4T1-EVs. In addition, we verified the stability of miRNAs loaded into eEV-PNCs and the change in release profile compared to miRNAs loaded in PLGA-NPs. We used antimiRNA-21 loaded PLGA-NP before and after extrusion using 4T1-eEV (eEV-PNC) for release by antimiRNA-21 quantification. The miRNA release profile from PLGA-NPs before and after eEV coating (eEV-PNC) exhibited similar trends in release profile over time (30 min to 24 h). In contrast, eEV-PNCs showed much lower release compared to PLGA-NPs. PLGA-NPs showed an initial release of 4.2% (30 min) and reached 12.5% by 24 h. In contrast, for eEV-PNC, the release started with 1.4% (30 min) and reached a maximum of 6.9% by 24 h (Figure S3, Supporting Information). In addition, we did not observe any change in the stability of antimiRNA-21 upon coating the PLGA-NPs using 4T1-eEVs. The change in release profile by eEV-PNCs could possibly be owing to the membrane coating associated blocking of mRNA release from the PLGA-NPs.

We further investigated our previously reported[28] proteomic profiles of SKBR3 cancer cell-derived extracellular vesicles (SKBR3-eEVs) and 4T1-eEVs with a focus on organotropism. We identified 1782 and 1910 proteins in each sample respectively, spanning over six orders of magnitude of protein abundance. 91% and 95% of the identified proteins were present in Vesiclepedia and ExoCarta respectively (**Figure 3**a), showing significant agreement with EV-associated proteins in the literature. We further investigated the involvement of these proteins in differential cancer cell-specific tropism, tumor cell communication, and cell–cell signaling by annotating identified proteins using the KEGG database into cell migration and cell-cell adhesion categories. 4T1-eEVs were found to be more versatile in terms of the number of different cell types with which they can interact, with the number of different proteins related to cell-cell adhesion proteins exceeding those identified in SKBR3-eEVs (35 vs 13 proteins) (Table S2, Supporting Information). Furthermore, the total amount of

MS signal derived from cell-cell adhesion proteins (2% vs 0.6%) also indicated that the detected signal from these proteins was at least three times more abundant in 4T1-EVs than in SKBR3-eEVs (Figure 3b). The interaction between cell adhesion molecules on the surface of 4T1-eEVs plays a key role in their organotropism. Investigation of cell migration-related proteins revealed similar proportions in terms of the number of identified proteins, 305 vs 117, and 16% vs 6% of the total MS signal when we compared 4T1-eEVs and SKBR3-eEVs, respectively. These results indicate that there were nearly three times more proteins involved in cell migration in 4T1-eEVs (Figure 3b). Similarly, there was substantially more MS signal associated with intracellular proteins such as nuclear, cytosolic, and other cellular compartments in SKBR3-eEVs than 4T1-eEVs (Table S3, Supporting Information). To better understand the role of the differences observed in cell–cell adhesion, we classified the identified cell adhesion molecules according to four group types: Ig-superfamily, claudins, integrins, and cadherins of 4T1-EVs (Figure 3c,d). The Z-score of intensity Based Absolute Quantification (iBAQ) showed that cadherin-1 and other Ig-superfamily adhesion molecules, such as VCAMI, GlgI, and Cntn1, were of low abundance on the surface of 4T1-eEVs. Some other specific Ig-superfamily adhesion molecules, such as CD9, CD44, CD47, CD81, CD82, CD276, and CD166, as well as claudins and integrins, were highly abundant on the surface of 4T1-eEVs.

In tumor-derived EVs, integrins are crucial in preparing a pre-metastatic tumor niche and guided organ-specific metastasis based on EV-cell tropism. The claudins play an important role in the formation and function of tight junctions. Several of these proteins are aberrantly expressed in cancer, including Cldn3, 4, and 7. Furthermore, we performed gene enrichment analysis of proteins identified in 4T1-eEVs against the whole mouse proteome database. Enriched categories were identified by gene ontology (GO) cellular component, GO biological process, and molecular function analysis (Figure 3e–h). The protein enrichment is represented as −log10 of *p*-value after Bonferroni correction. Interestingly, the GO based cellular component analysis revealed that most 4T1-eEVs proteins belong to plasma membranes followed by the proteins localized in the cytoplasmic compartment, and a minor contribution from the nuclear compartment (Figure 3e). These findings further confirm that the 4T1-eEVs were highly enriched with proteins belonging to the 4T1-plasma membranes, and our standard EV production process yielded CCDVs with minimal contamination by other cellular compartment materials. Together with the proteomic analyses, our experimental data demonstrated that 4T1-eEVs were proteo-lipid vesicles, highly enriched with 4T1 cell surface adhesive proteins that likely contributed to homologous tumor-specific adhesion.

After this extensive characterization of 4T1-eEVs, we next formulated 4T1-eEVs-PNCs by fusing eEVs with pre-formulated PLGA-NCs loaded with either antimiRNA-21 or antimiRNA-10b (**Figure 4**a) as reported previously.[26] The encapsulation efficiencies of both antimiRNA-21 and antimiRNA-10b in PLGA-NCs in different batches were consistent and were in the range of 65–75%. DLS and NTA analyses showed that the 4T1-eEVs functionalization of the different nanoformulations of PLGA-antimiRNA-21 or PLGA-antimiRNA-10b slightly increased the particle size to 10–20 nm while reducing the surface zeta potentials as shown in Figure 4b,c, and Table S1, Supporting Information. Additionally, TEM micrographs also confirmed the formation of a hybrid core-shell nanosphere consisting of a PNC nanocore wrapped by a thin lipid layer (Figure 4d), which was consistent with earlier reported typical core-shell NCs.[29,30] These results were further confirmed by confocal microscopy as the presence of DiD (red) and NBD-PC (green) signals perfectly corresponded to the PNC and eEV portions of 4T1, respectively (Figure 4e). We have previously reported that 4T1-EVs functionalization on gold-iron-oxide hybrid metallic NPs enables greater uptake by homologous and uPAR positive 4T1 and MDA-MB-231 cancer cells, while showing minimal uptake with NIH 3T3 fibroblast cells (Figure S4, Supporting Information).[26] From these results we deduced that CCAMs play a role in NP uptake by cancer cells.[26] However, it was important to determine whether bioengineered uPA peptide on the 4T1-eEVs-PNCs that target the uPAR can enhance receptor-mediated NCs uptake. Therefore, we performed in vitro uptake assays using Celigo imaging cell cytometry (Figure S5, Supporting Information) using 4T1 cells, as these cells are known to overexpress uPAR. We treated 4T1 cells with uPAR-small interfering RNA (siRNA) and scrambled siRNA to evaluate the role of uPA-uPAR interactions in TNBCs. As anticipated, the incubation of the eEVs-uPA-PLGA-antimiRNA-21-Cy5 with scrambled siRNA treated 4T1 cells (Figure 4f,g) showed significant increase in uptake when compared to Sc-uPA-PLGA NPs (*t*-test, $***p < 0.0001$) and this uptake effect was abrogated in the uPAR siRNA treated 4T1 cells, confirming that the NPs uptake was uPAR receptor-mediated (Figure S6, Supporting Information). Moreover, in the siRNA-treated group, incubation of eEVs-uPA-PLGA-antimiRNA-21-Cy5 and Sc-uPA-PLGA-antimiRNA-21-Cy5 NCs showed relatively equal uptake (not significant) and nearly twofold higher uptake (*t*-test,$** p < 0.009$) than uncoated PLGA-antimiRNA-21-Cy5 NPs. This particular result confirmed that the 4T1-eEVs functionalization onto the nanocarrier enhanced the NPs uptake as reported previously.[26]

A combination of different therapeutic strategies could have great potential to effectively treat TNBCs by taking advantage of their synergetic effects. We and others have previously shown that the therapeutic efficacy of NPs-mediated co-delivery of antisense miRNAs can be enhanced synergistically with low-dose chemotherapeutics (e.g., doxorubicin, DOX). However, to effect the controlled release of desired therapeutic miRNAs from a co-loaded nanosystem is much more challenging than the controlled release of miRNA from individually loaded NPs. Therefore, we formulated different NPs (Table S1, Supporting Information) and tested their synergistic activity with low-dose DOX by preparing a nanococktail mixture. We theorized that low-dose DOX would serve to inhibit the cell cycle and slow down the rate of cell division. Hence, we next assessed the synergistic therapeutic enhancement of low-dose DOX with a cocktail mixture of Sc-uPA or uPA-4T1-eEV-PNCs loaded with either antimiRNA-21 or antimiRNA-10b. The uPAR targeted uPA nanococktail mixture showed a significant antiproliferative effect in response to the treatment with free DOX (2.8-fold) and control cells (3.2-fold, $p < 0.01$) (Figure 4h). The uPAR targeted uPA nanococktail mixture caused significantly higher cytotoxicity (2.2-fold, $p < 0.01$) on 4T1 cells, when compared to non-uPAR targeted Sc-uPA-nanococktail formulations (Figure 4h). Further, treatment with uPAR targeted individual eEV-uPA-PLGA-antimiRNA-21 (1.9-fold, $p < 0.01$) or eEVs-uPA-PLGA-antimiRNA-10b (1.7-fold,

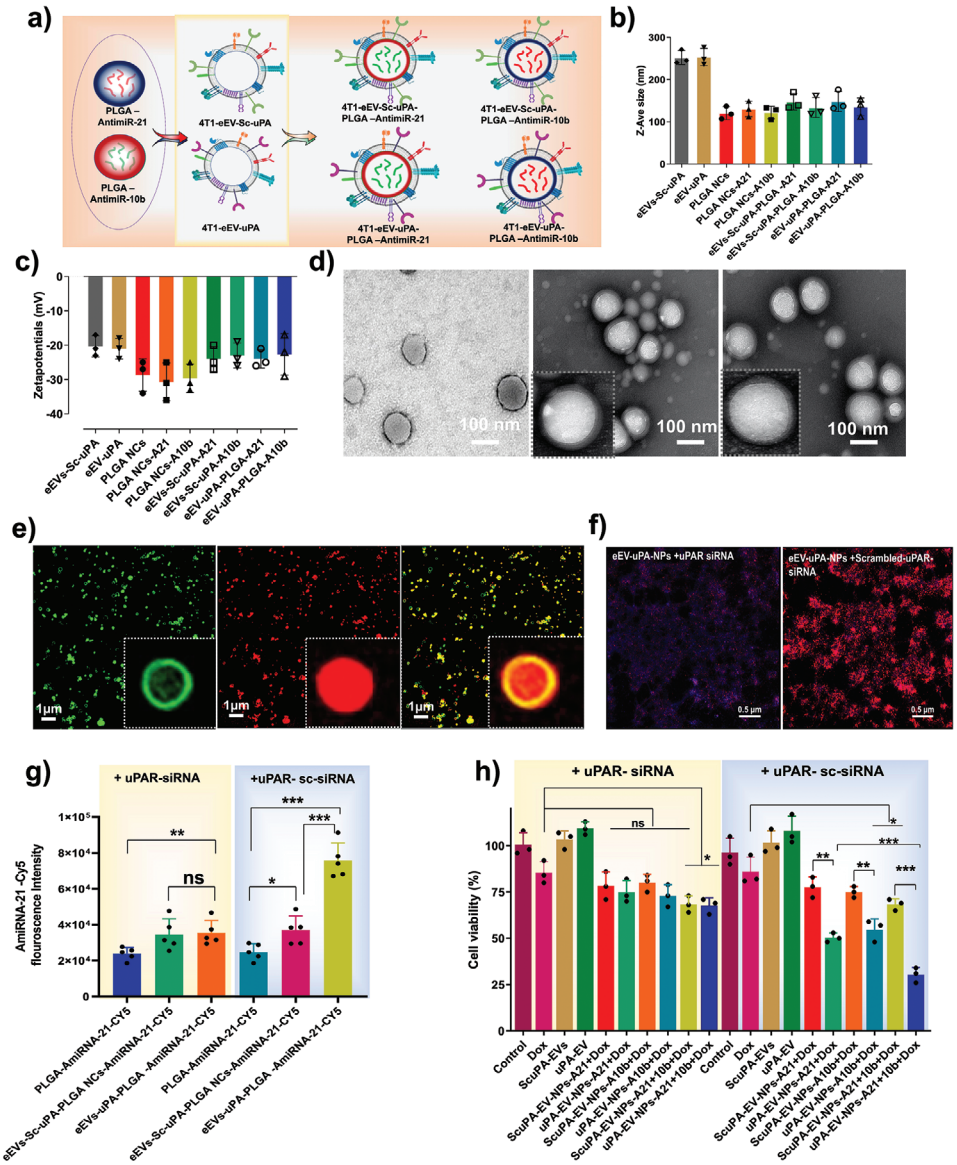

Figure 4. a) Schematic diagram shows the uPA and Sc-uPA peptide displaying 4T1-eEVs functionalized PLGA- nanocarriers loaded with antimiRNA-21 and antimiRNA-10b. b) Characterization of 4T1-eEV functionalized PLGA- nanocarriers by DLS analysis shows the comparative size distribution of 4T1-eEVs and eEVs functionalized nanoformulations ($n = 3$). c) Zeta sizer-based surface charge analysis shows the comparative charge analysis between 4T1-eEVs and eEVs functionalized nanoformulations ($n = 3$). d) Transmission electron micrograph shows the PLGA nanocarrier and 4T1-eEVs coated PLGA-P NPs. Negative-stain electron microscopy was performed to visualize the eEVs on the PLGA- NCs. Scale bars, 100 nm. Insert figures within this panel showing the higher magnification images of hybrid polymeric nanocore and the proteo-lipid shell of eEV-PLGA. e) Confocal laser scanning microscopy images showing the hybrid nanopolymeric core (DiD) and shell (NBD-PC-green) (Scale bar, 1µm). Investigation on the uPAR targeted uptake of uPA peptide displaying 4T1-eEV functionalized PLGA nanocarriers. Insert figures within this panel showing the higher magnification image of proteo-lipid shell of eEVs labeled with NBD-PC, polymeric nanocore labeled with DiD, and the merged image of core-shell hybrid ($n = 3$). f) Fluorescence microscopy images show the uPAR targeting capability of uPA peptide displaying 4T1-eEV functionalized PLGA-nanocarriers loaded with antimiRNA-21-Cy5, g) quantitative data shows the uPAR targeting efficiency of uPA peptide displaying 4T1-eEVs functionalized PLGA- nanocarriers. The fluorescence images were acquired with an excitation at 650 nm and emission at 670 nm using a Celigo Imaging Cytometer (Nexcelom Bioscience, LLC, MA) ($n = 3$). Incubation of the eEVs-uPA-PLGA-antimiRNA-21-Cy5 with scrambled siRNA treated 4T1 cells showed significantly higher uptake when compared to Sc-uPA-PLGA-antimiRNA-21-Cy5 NPs, and this uptake effect was abrogated in the uPAR siRNA treated 4T1 cells. In the siRNA-treated group, incubation of eEVs with uPA and Sc-uPA-PLGA-antimiRNA-21-Cy5 NPs showed relatively equal uptake (not significant), and showed comparatively higher uptake than uncoated PLGA-antimiRNA-21-Cy5 NPs. In vitro cytotoxicity assay. h) CCK8 assay showing that the targeted combinational therapy, namely cocktail mixture of 4T1-eEV-uPA-PLGA-antimiRNA-21 and 4T1-eEV-uPA-PLGA-antimiRNA-10b with a combination of low dose DOX resulting in a significant antiproliferative effect compared to cells treated with free DOX (2.8-fold) and control cells. The uPAR targeted combinational nanococktail mixtures (uPA-4T1-eEVs-PNCs-AntimiRs) with low dose DOX caused significantly higher cytotoxicity (2.2-fold, $p < 0.01$) in 4T1 cells, when compared to non-uPAR targeted Sc-uPA-nanococktail formulations with low dose DOX. Similarly, treatment with uPAR targeted individual nanoformulations eEV-uPA-PLGA-antimiRNA-21 or eEVs-uPA-PLGA-antimiRNA-10b nanoformulations alone in combination with low dose DOX produced considerable cytotoxicity in 4T1 cells, compared to untreated control 4T1 cells and low dose DOX alone treatments. (*t*-test, $*p < 0.01$, $**p < 0.001$, and $***p < 0.0001$).

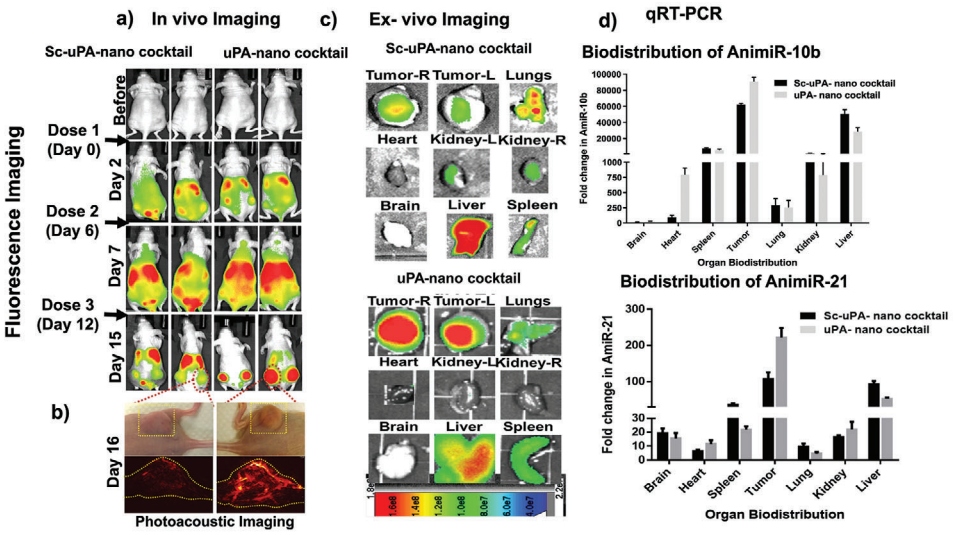

Figure 5. In vivo biodistribution and uPAR targeted accumulation of eEVs functionalized PLGA-antimiRNA nanococktail in syngeneic 4T1 subcutaneous tumors in nude mice (nu nu^{-1}). a) In vivo fluorescence imaging showed the whole-body biodistribution and 4T1-tumor specific accumulation of ICG labeled Sc-uPA and uPA nanococktail formulations administered via tail vein injection on Days 0, 6, and 12, and imaged on Days 2, 7, and 15 using a Lago (Spectral Imaging system) in vivo imaging system. b) Photoacoustic imaging of 4T1 tumors for the accumulation of ICG labeled eEV-uPA-PLGA-antimiRNAs on Day 16. c) Ex vivo fluorescence imaging showed the uPAR mediated 4T1 tumor-specific accumulation of eEV-uPA-PLGA-antimiRNA-21 nanococktail formulations on Day 17. The uPA and Sc-uPA nanococktail formulations injected nude mice were sacrificed on Day 17, and the organs (liver, spleen, kidneys, heart, lungs, and brain) were collected for ex vivo imaging. d) The biodistribution and tumor-specific accumulation of ICG, antimiRNA-21, and antimiRNA-10b in nude mice injected with uPA and Sc-uPA functionalized eEV-PLGA-antimiRNA-21 nanococktail formulations. Lago fluorescence imaging and TaqMan real-time qRT-PCR were used for organ-specific biodistribution based on the quantification of ICG and antimiRNAs. The endogenous expression of sno234 was used as an internal control to normalize the qRT-PCR results. We used five animals ($n = 5$) in each group while repeating the experiment twice in the study ($n = 10$).

$p < 0.01$) nanoformulations alone in combination with low dose DOX produced considerable cytotoxicity in 4T1 cells, compared to untreated control 4T1 cells and low dose DOX alone treated cells (Figure 4h). These findings indicated that the uPAR targeted uPA nanococktail can enhance the therapeutic efficacy of antimiRNAs by its unique synergistic mechanism. The Sc-uPA nanococktail mixture also showed considerable cytotoxicity (1.4 -fold, $p < 0.01$), compared to the control cells and low-dose DOX alone treatments. This antiproliferative effect was particularly abrogated by pretreating 4T1 cells with uPAR-siRNA, which further confirmed that the observed cytotoxicity was mediated by an uPA–uPAR assisted antiproliferative effect of the nanoformulations (Figure 4h). It is also noteworthy that the 4T1-eEVs alone and low dose DOX alone treatments did not cause any substantial cytotoxicity in 4T1 cells, signifying that the observed anticancer effects were owing to the inhibition of endogenous oncomiRs such as miRNA-21 and miRNA-10b in 4T1 cells. Overall, the higher antiproliferative effects of the uPA-nanococktail mixture compared to that of the non-targeted Sc-uPA-nanococktail mixture were likely owing to the encapsulation and extended antimiRNAs released from the biodegradable polymeric nanocarrier, which maintain the availability of stable and active antimiRNAs and result in a sustained functional effect.

After the in vitro study, we initially evaluated the whole-body biodistribution and tumor-specific tropism of uPAR targeted uPA and Sc-uPA nanococktail mixtures in 4T1 tumors in nude and immunocompetent mouse models (Figure S7, Supporting Information). To visualize the biodistribution and ex vivo imaging of both nanococktails, we used sensitive and intrinsic NIR fluorescence imaging (NIRF) of indocyanine green (ICG) by conjugating NH_2 reactive ICG to 4T1-eEV-PNCs (Figure S8, Supporting Information). After conjugation, we measured ICG fluorescence using an optical imaging system along with an ICG standard graph to quantify the conjugated ICG to EV proteins (Figure S9a, Supporting Information). We also further confirmed the conjugation efficiency of ICG to the EV proteins by optical imaging after resolving the proteins in 4–12% SDS-PAGE (Figure S9b–d, Supporting Information). We found that each dose of eEV-PNC injection contained an estimated protein equivalent of 90 ± 5 µg, and ICG equivalent of 14.4 ± 2 µg in a 150 µL eEV-PNC dose (Table S1, Supporting Information). **Figure 5**a shows whole-body IVIS imaging of ICG fluorescence signals captured from the 4T1 tumor-bearing nude mice. We observed (Figure 5a) that after the first dose of the nanococktail injection, the fluorescence intensity of ICG initially accumulated in the reticuloendothelial system, specifically in the regions of the liver and spleen. Interestingly, the uPAR targeted uPA-nanococktail formulations showed more rapid tumor-specific accumulation than non-uPAR targeted Sc-uPA nanococktail formulations (Figure S10, Supporting Information). As the study periods were extended for the second and third doses, the uPAR targeted NPs continuously accumulated at the tumor sites and exhibited apparent fluorescence signals in the tumors, indicating a distinctive targeting ability of the uPA nanococktail formulations (Figure 5a and Figure S10, Supporting Information). Relatively strong fluorescence was observed after six days, while fluorescence signals from other organs began to disseminate toward the tumors signifying a uPA-mediated uPAR targeted accumulation of uPA-nanococktail

formulations. On Day 15, both uPA and Sc-uPA-nanococktail formulations exhibited tumor accumulations, however, the uPA-nanococktail formulations showed an enhanced time-dependent tumor accumulation at the right and left 4T1 tumor sites as indicated by the strong ICG fluorescence signals (Figure 5a). These findings stress that uPA-mediated uPAR targeted delivery of NPs can accumulate more intensely at tumor sites compared to the Sc-uPA targeted nanococktail. To further validate these observations, we performed photoacoustic imaging (PAI) on Day 16, as ICG can be used as a PAI contrast agent. As shown in Figure 5b, the PAI signals of ICG were increased dramatically in uPAR targeted uPA-nanococktail formulation treated mice than in the non-targeted Sc-uPA-nanococktail formulations administered group. Moreover, PAI further confirmed that the injected uPA-nanococktail formulations penetrated deeply inside the tumor interstitium, compared to the non-targeted Sc-uPA nanoformulations (Supporting Movies S1, 2, 3 and 4). We further assessed the biodistribution of NPs using *ex vivo* imaging of harvested organs and tumors on Day 17 (Figure 5c). We observed that the fluorescence intensity of ICG was higher in the right and left tumors of uPAR targeted uPA-4T1-eEVs-PNCs nanococktail formulation injected group compared to the non-targeted Sc-uPA-4T1-eEVs-PNCs formulations injected group. In other organs (heart, lungs, liver, spleen, and kidneys), the uPAR targeted NPs group showed a minimal ICG-fluorescence intensity compared to that in the non-uPAR targeted group (Figure 5c). Overall, the ICG-fluorescence intensity was considerably higher for the non-uPAR targeted NPs group than uPAR targeted group.

Next, we assessed the distribution of delivered antimiRNA-21 and antimiRNA-10b in tumors and major organs using quantitative RT-PCR. For antimiRNA-21 or antimiRNA-10b quantification, the mice were sacrificed, and major organs were collected and used for total RNA extraction. As expected, a significant amount of uPAR targeted uPA-4T1-eEVs-PNCs nanococktail formulations mediating the delivery of antimiRNA-21 and antimiRNA-10b was distributed in 4T1 tumors as compared to non-targeted Sc-uPA-4T1-eEV-PNCs formulations mediated delivery, signifying the advantages of uPA-mediated uPAR targeting in TNBC therapy (Figure 5d). We also found a considerable amount of non-targeted Sc-uPA-4T1-eEV-PNCs mediated antisense-miRNA delivery to tumors (Figure 5d). We speculate that this is likely owing to the homologous adhesion of cancer cell surface adhesive proteins, the integrins of 4T1-eEVs, possibly playing a role in this tumor-specific accumulation. Additionally, a considerable amount of antisense-miRNA delivered using eEV-PLGA nanoformulations also accumulated in other organs including the liver, spleen, heart, and kidneys, which is likely owing to the 4T1-EV binding to the extracellular proteins, specifically integrin receptors, but this observation requires further investigation. Overall, our IVIS and PAI experimental data suggested that bioengineered uPA-4T1-eEVs functionalization on PNCs-mediated delivery of antimiRNAs can enable specific recognition of its uPAR target in 4T1 tumors in vivo.

We further compared the tumor-targeting ability and the uPAR targeted combinational therapeutic enhancement of uPA-4T1-eEVs-PNCs in immunocompetent BALB/c mice (Figure S7, Supporting Information). Similar to nude mice, the ICG labeled uPA and Sc-uPA-4T1eEV-PNCs nanococktail mixtures were injected intravenously into tumor-bearing mice. After the first dose, the results showed earlier accumulation of uPA-4T1-eEVs-PNCs nanococktail mixtures in the right and left 4T1 tumors when compared to non-uPAR targeted Sc-uPA-4T1-eEVs-PNCs formulations (**Figure 6**a). As study periods were extended for the second and third doses, the uPAR targeted uPA-4T1-eEV-PNCs nanococktail formulations that continuously accumulated at tumor sites exhibited apparent ICG fluorescence signal, indicating a distinctive targeting capability of uPA-eEV-PNCs formulations (Figure 6a). Comparatively, a strong and early fluorescence was observed after six days, while the ICG fluorescence signals from other parts of the body began to disseminate toward the 4T1 tumors, validating the uPAR targeted migration of uPA-4T1-eEV-PNCs (Figure 6a). On Day 15, both uPA and Sc-uPA nanoformulations displayed tumor accumulations, however, uPAR-targeted nanoformulations showed an enhanced time-dependent tumor accumulation at the tumor sites as indicated by the strong ICG fluorescence intensity at the tumors when compared to the Sc-uPAR targeted formulations (Figure 6a). To further validate these observations, we performed ex vivo imaging of harvested organs and tumors on Day 17. That showed fluorescence intensity of ICG was higher in the right and left tumors of the uPAR targeted NPs injected group compared to the Sc-uPAR targeted nanoformulations (Figure 6b). The uPAR targeted NPs group showed minimal ICG-fluorescence intensity in the heart, lungs, kidneys, liver, and spleen when compared to that in the Sc-uPAR targeted group (Figure 6b). Specifically, the ICG-fluorescence intensity was considerably higher for the Sc-uPAR targeted NPs group than uPAR targeted NPs group. Moreover, qRT-PCR analysis further confirmed that a substantial amount of uPAR-targeted nanoformulations mediated delivery of antimiRNA-21 and antimiRNA-10b accumulated at tumor sites when compared with non-targeted nanoformulations mediated delivery, signifying the potential use of uPA-4T1-eEV-PNCs mediated delivery of antimiRNAs for cancer therapies (Figure 6c). Our experimental data also showed that a considerable amount of non-targeted nanoformulations-mediated antimiRNA delivery accumulated in the 4T1 tumors, emphasizing the advantages of homologous cancer cell membrane functionalization on the NPs. Furthermore, an extensive amount of antimiRNAs delivered using 4T1-eEV-PNCs also accumulated in other organs including the liver, spleen, heart, and kidneys, which is likely owing to the 4T1-EV binding to the extracellular proteins, specifically integrin receptors, but this observation requires further investigation.[31] This could be partially owing to the presence of some PLGA NPs without membrane, on account of the low efficiency of the extrusion process used for coating. This could be improved by future enhancement of membrane coating. This would likely eliminate the immune recognition of eEV-PNCs by macrophages and their accumulation in non-target organs.

The quantitative fluorescence analysis of tissues ex vivo for the delivered ICG-PNCs at the end point clearly showed that the uPA-PNCs accumulated more in tumor tissues compared to mice receiving Sc-uPA-PNCs. The uPA-4T1-eEV-PNCs were more numerous in tumors compared to other clearance organs (liver and spleen). It is likely that because the *ex vivo* images were taken at the end point of the study when mice had received three doses of PNCs. Furthermore, the clearance rate of injected PNCs by tumors may be much slower compared to liver and spleen. Also, in contradistinction to liver and spleen, tumors

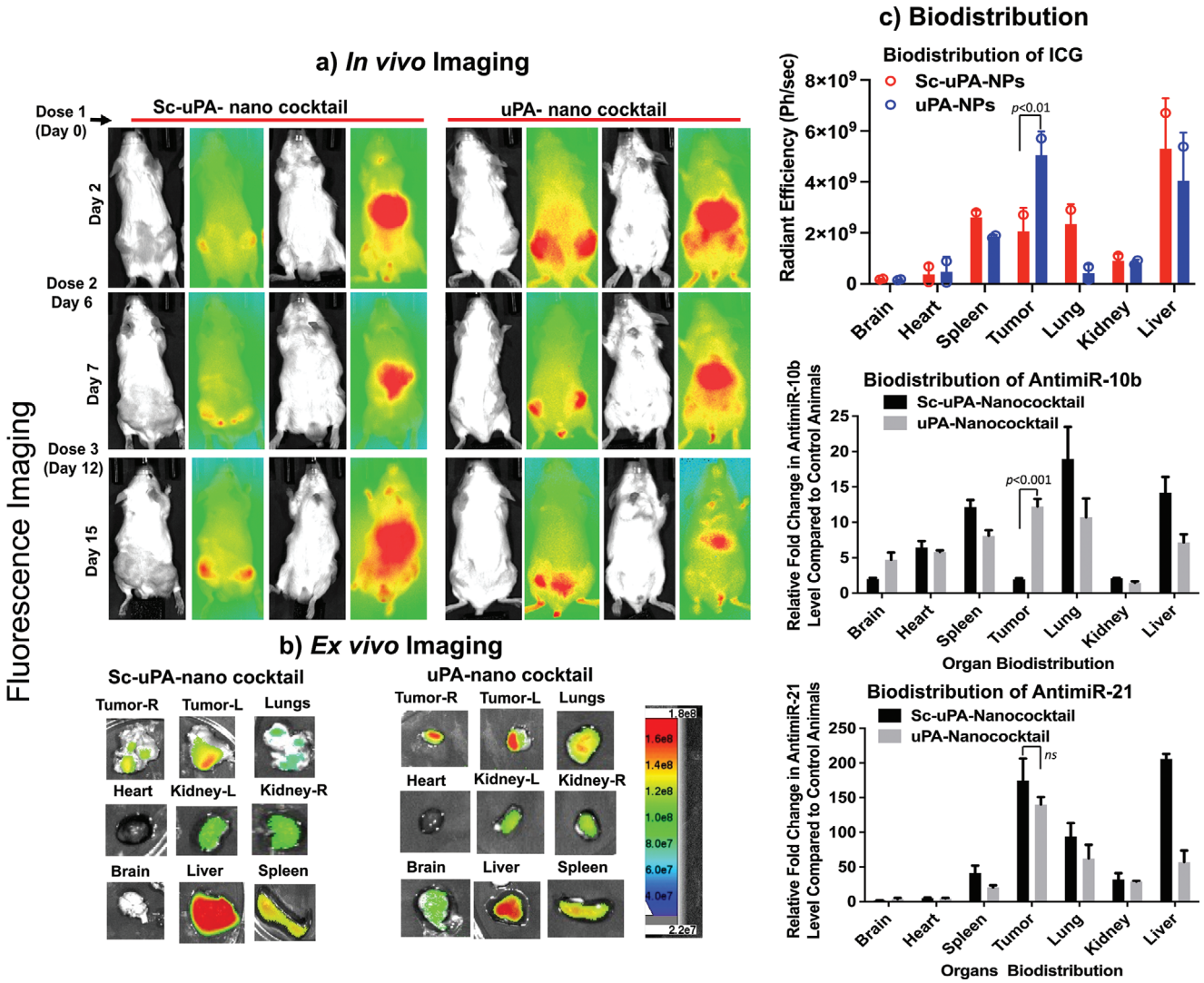

Figure 6. In vivo biodistribution and uPAR targeted accumulation of eEVs functionalized PLGA-antimiRNA nanococktail in syngeneic BALB/cJ mice bearing 4T1 subcutaneous tumors. a) In vivo fluorescence imaging shows the whole-body biodistribution and 4T1-tumor specific accumulation of ICG labeled uPA and Sc-uPA nanococktail formulations administered via tail vein on Days 0, 6, and 12, and imaged on Days 2, 7, and 15 using a Lago (Spectral Imaging system) imaging system for ICG fluorescence. b) Ex vivo fluorescence imaging shows the uPAR mediated 4T1 tumor specific accumulation of uPA nanococktail formulations in BALB cJ^{-1} mice bearing syngeneic 4T1 subcutaneous tumors. The uPA and Sc-uPA nanococktail formulations injected nude mice were sacrificed on Day 17, and the organs (liver, spleen, kidneys, heart, lungs, and brain) were collected for ex vivo imaging analysis. c) The biodistribution and tumor specific accumulation of ICG, antimiRNA-21, and antimiRNA-10b delivered using uPA and Sc-uPA nanococktail formulations injected in BALB cJ^{-1} mice bearing 4T1 subcutaneous tumors. Lago fluorescence imaging and Taqman real-time qRT-PCR were used for the organ-specific biodistribution based on the quantification of ICG and antimiRNAs. The endogenous expression of sno234 was used as an internal control to normalize qRT-PCR results. We used five animals ($n = 5$) in each group while repeating the experiment twice in the study ($n = 10$).

retain PNCs through eEV-mediated cellular adhesion proteins and uPA-mediated targeting to the tumor tissues. All these factors could have contributed for higher amounts of ICG fluorescence signal in tumors.

The overall survival (OS) results revealed that treatment using the uPA nanococktail mixture led to a robust antitumor response, as these nanoformulation mixtures significantly improved the OS of syngeneic 4T1 tumor-bearing immunocompetent mice ($n = 10$). Seven mice showed progression-free survival, and among them, four mice (40%) showed complete tumor elimination by the end of the study (**Figure 7** and Figure S7, Supporting Information). Additionally, the median OS time for the uPAR-targeted uPA nanococktail mixture was significantly different ($p < 0.01$) from treatment using the Sc-uPA-nanococktail mixture, or saline ($p < 0.0001$), or the low dose DOX alone treated groups ($p < 0.0001$). Interestingly, treatment with the Sc-uPA-nanococktail mixture exhibited an intermediate antitumor effect, as this nanoformulation mixture increased the median OS to 59.5 days and three mice showed progression free survival (PFS) at Day 90, which is significantly higher ($p < 0.0001$) than saline (median OS of 21 days) and low dose DOX alone treated groups (median OS of 33 days) (Figure 7a). EVs derived from cancer cells

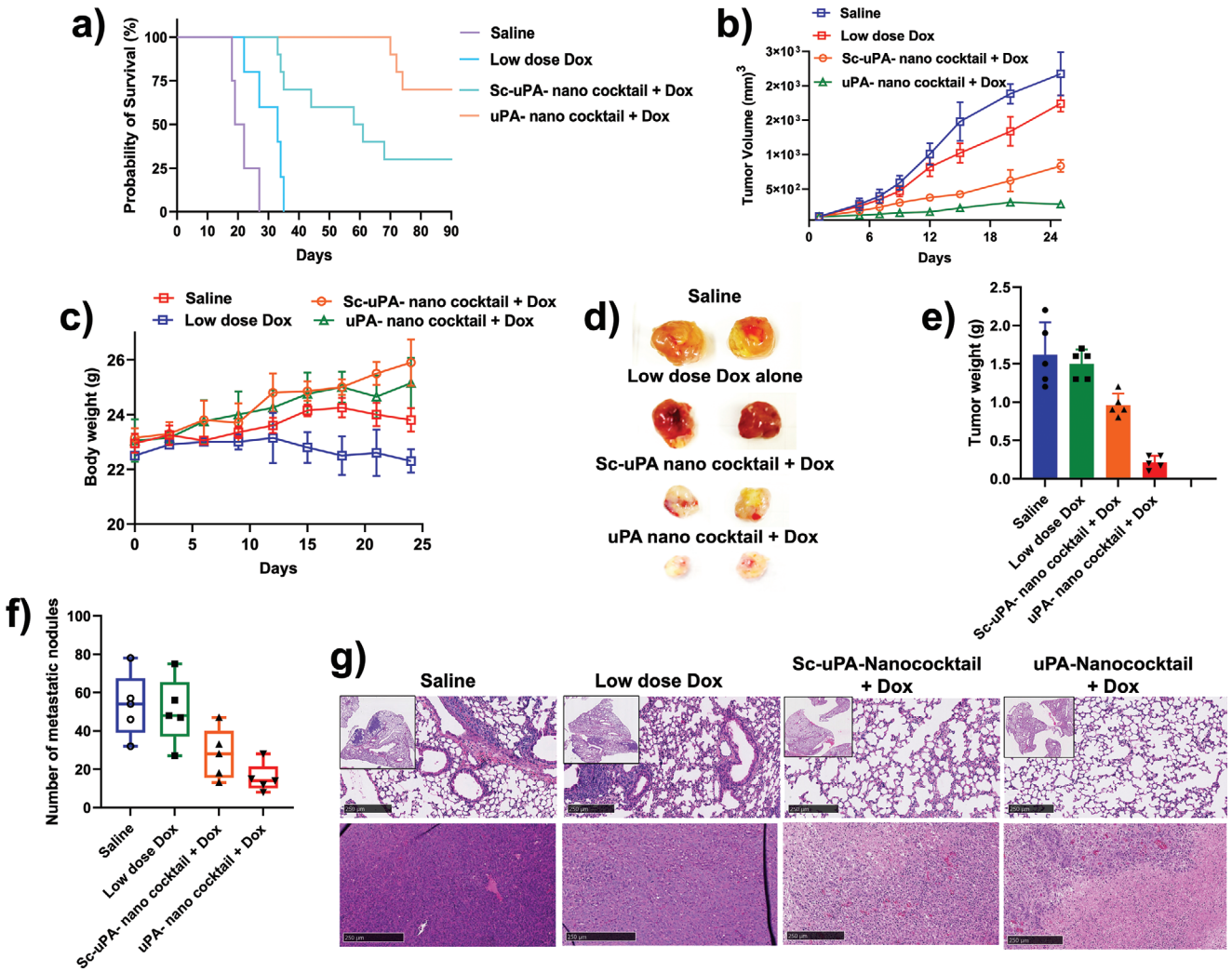

Figure 7. **a)** Survival curves of mice bearing 4T1 tumors given different treatments (Saline; Low dose DOX alone; Sc-uPA nanococktail; and uPA nanococktail). We used ten animals in each group for assessing the survival rate ($n = 10$). b) 4T1 tumor growth kinetics after different treatments. c) Body weight of mice receiving different treatments. d) Ex vivo images of tumors excised one month after treatments. e) Excised tumor weights were measured a month after treatments. f) The number of metastatic nodules in the lungs after different treatments. g) Histologic assessments of lungs and tumors using H&E staining in mice. Top panel: representative images of lung tissues in various treatment groups showed the metastatic nodules at the end of the experiment. Figure inserts within this panel showing the respective low magnification images of lung metastatic foci of 4T1 tumor under different treatment conditions. Bottom panels: representative H&E staining of tumor sections in various treatment groups. Scale bars, 250 μm. Data are means ± SD. Statistical significance was calculated by *t*-test (* $p < 0.05$, ** $p < 0.01$, *** $p < 0.001$).

maintain their natural affinity (4T1-EVs mediated homologous adhesive proteins) to source cells. Hence, the NPs coated using EVs derived from 4T1 cells stably expressing Sc-uPA maintain the original source cell surface property and demonstrate therapeutic properties, which are enhanced upon use of eEV-PNCs derived from cells expressing uPA. The results shown in Figure 7a confirm this, where the animals receiving Sc-uPA-PNC showed intermediate antitumor effects compared to other control groups. Furthermore, we found that the uPAR targeted uPA nanococktail mixture steadily delayed the tumor growth compared to other treatments (Figure 7b and Figures S11–S13, Supporting Information) with negligible systemic toxicity (Figure 7c and Figure S14, Supporting Information). The uPA-nanococktail mixtures also showed robust inhibitory effects on metastatic 4T1 tumor nodules in the lungs compared to control groups (Figure 7f,g).

In summary, here we investigated the targetability and therapeutic enhancement of uPAR targeted uPA and Sc-uPA tumor cell derived eEV coated PNC nanococktail formulations for targeted combinational TNBC therapy in tumor bearing nude and immunocompetent mouse models. Functionalization of antimiRNA-loaded PNCs with eEVs displayed uPA peptides that showed a robust tumor tropism. Furthermore, uPA-nanococktail mediated combinational antimiRNA-21 and antimiRNA-10b delivery resulted in a higher accumulation of nanococktail in tumor tissues, and in that way, it synergized the antiproliferative effects of low dose DOX. Collectively, treatment of tumor-bearing mice using uPA nanococktail formulations reliably delayed

tumor growth and significantly ($p < 0.01$) improved the overall survival rate of mice while showing complete tumor elimination in 40% of mice by the end of the study compared to other treatment conditions. This treatment approach also showed negligible systemic toxicity in immunogenic BALB/c mice bearing 4T1-tumors. Furthermore, our targeted nanococktail approach shows several advantages over conventional drug monotherapy and investigational nanotherapy, including cancer cell-derived vesicles coated nanocarriers. First, combinational cancer therapy is a keystone of cancer therapy. Here, we formulated nanococktail mixtures that contain uPAR targeted uPA peptide or scrambled-uPA peptide displaying 4T1-eEVs coated NPs, separately loaded with either antimiRNA-21 or antimiRNA-10b and investigated their synergistic effects with low dose chemotherapeutics. This amalgamation of uPAR targeting and individual anti-miRNA-loaded nanoformulation mediated anticancer therapy enhances the therapeutic efficacy in a significant manner when compared to conventional monotherapy approaches. The targeting of multiple cell signaling pathways synergistically results in a lower required therapeutic dosage of each antimiRNA or chemotherapeutic drug. Second, this "nanococktail approach" can be further expanded by mixing multiple nanoformulations loaded with different drugs, genes, and nanoprobes for simultaneous early cancer diagnosis, therapy, and treatment monitoring. Third, our bioengineering and peptide-mediated targeting strategy can be readily translated to the clinic by using autologous tumor cells that have the flexibility for ex vivo expansion and genetic engineering. Finally, once translated clinically, our bioengineered cell-free therapeutic strategy could be more cost-effective and less time-consuming than commercial cell therapeutics, which require labor-intensive, high-cost, and time-uncontrollable processes.

3. Experimental Section

Materials: Poly (D,L-lactide-*co*-glycolide) (50/50) was purchased from Sigma-Aldrich (St. Louis, MO, USA). Cy5-labeled anti-miR-21, anti-miR-21, and anti-miR-10b RNA oligos were obtained from PAN Facility at Stanford University, at the purity of above 95%. All other chemicals and reagents of analytical grade or above from were purchased Sigma, as well as cell-culture plates, FBS, penicillin, streptomycin, sodium bicarbonate, cell-culture medium, and PBS from GIBCO BRL (Frederick, MD).

Methods: *Cell Culture*: Human breast adenocarcinoma (MDA-MB-231), mouse breast cancer cells (4T1), human glioblastoma cells (U87), human hepatocellular carcinoma cells (HepG2), and human breast cancer cells (SKBR3) were cultured in Dulbecco's modified Eagle's medium (DMEM) supplemented with 10% fetal bovine serum (FBS), 100 U mL^{-1} penicillin, and 0.1% streptomycin, and maintained at 37 °C and 5% CO_2. Sublines generated from these cell lines were cultured in the same manner.

Plasmid Construction: All plasmids were constructed using standard molecular cloning methods. pDisplay vector was obtained from Thermos Fisher scientific. The uPA peptide sequence (VSNKYFSNIHWGC) and the scrambled peptide (Sc-uPA) sequence (YKNNFISGHVSCW) flanked by BgIII/SalI restriction sites was generated by synthesizing overlapping primers and by annealing to generate double-stranded DNA with overhang cohesive ends of restriction enzymes. The annealed fragments were then cloned into respective enzyme digested vector backbones. Sequence confirmed positive clones were used for stable cell generations and further experiments.

Engineered Extracellular Vesicles Production from Urokinase-Type Plasminogen Activator Peptide (uPA pep) and Scrambled uPA Peptide (Sc-uPA-pep) Expressing 4T1 Stable Cells: Engineered extracellular vesicles were produced from urokinase-type plasminogen activator (uPA peptide) and scrambled urokinase-type plasminogen activator peptide (Sc-uPA-peptide) expressing 4T1 stable cells. Briefly, constructs containing the genes for uPA, and Sc-uPA were transferred into 4T1 cells using Lipofectamine 2000 reagent (Invitrogen). Clones stably expressing the genes with 200 ng mL^{-1} Puromycin were then selected. After the selection of uPA or Sc-uPA stably expressing 4T1 cells, the EV isolation procedure proceeded as reported previously.[26,32,33].

Production and Characterization of Engineered Extracellular Vesicles (eEVs) Coated PLGA Nanocarriers Independently Loaded with Either Antisense miRNA-21 or Antisense miRNA-10b: The antisense-miRNA-10b and antisense-miRNA-21 independently encapsulated PLGA-nanocarriers were prepared via a modified double-emulsion solvent evaporation method as described by Devulapally et al.[17] The purified engineered extracellular vesicles (4T1-eEVs) were fused with PLGAanti-miR-21/anti-miR-10b by physical extrusion as described previously.[26] The mean particle diameter (z-average), size distribution (polydispersity index), and the surface charge (the ζ-potential) of uncoated and eEV coated NPs were analyzed using Zetasizer-90 (Malvern Instruments, Worcestershire, United Kingdom) (Malvern Instruments, Malvern, U.K.).[17,23] Nanoparticle tracking analysis (NTA) measurements were performed using a Nano sight NS300 (Malvern Instruments). For each sample, the authors took and analyzed at least five videos of 30–60 s with >200 detected tracks per video, and in at least one dilution, using the Nanoparticle Tracking Analysis software with default settings. All procedures were performed at room temperature. Transmission electron microscopy (TEM) images of the PNCs and eEVs coated-PNCs were obtained using FEI-Tecnai G2 F20 X-TWIN operated at an acceleration voltage of 200 kV, and images taken by an ORIUS CCD camera through Digital Micrograph.[33] For confocal laser scanning microscopy, 2 µg of DiD dye was added to the organic solution before PNCs core synthesis. Similarly, to elucidate the core–shell structure of 4T1-eEV-PNCs, NBD-PC were incorporated into eEVs, and then fused with DiD-loaded PNC cores. Images were acquired using a confocal microscope (TCS SP8 II, Leica, Heidelberg, Germany) equipped with a 63× oil-immersion objective and running the Leica LAS AF Ver 2.6 software. For confocal laser scanning microscopy, 2 µg of DiD dye was added to the organic solution before PNCs core synthesis. Similarly, to elucidate the core-shell structure of 4T1-eEV-PNCs, we incorporated NBD-PC into eEVs, and then fused with DiD-loaded PNC cores. Images were acquired using a confocal microscope (TCS SP8 II, Leica, Heidelberg, Germany) equipped with a 63× oil-immersion objective and running the Leica LAS AF Ver 2.6 software (Fuji photo film, Tokyo, Japan).[29]

Stability and Release Profile of miRNAs in 4T1-eEV-PNCs: The stability of miRNAs loaded in eEV-PNCs and the change in release profile compared to miRNAs loaded in PLGA-NPs were verified. antimiRNA-21 loaded PLGA-NPs before and after extrusion were used using 4T1 eEVs (eEV-PNCs). miRNAs in a time-dependent manner was collected by dialysis under physiological conditions. The release of miRNA was measured by using TaqMan quantitative RT-PCR. Samples were collected over 24 h. The total amount of loaded miRNA in PLGA-NPs and eEV-PNCs was quantified, and the miRNA was released in the medium using TaqMan qRT-PCR. The measured miRNA at each time point was denoted in terms of percentage total miRNA loaded in PLGA-NPs and eEV-PNCs.

ICG Dye Conjugation to EVs and Injected Dose Evaluation: The authors used amine reactive ICG for the conjugation of EVs isolated from 4T1 cells engineered to express uPA and Sc-uPA. The EVs of 1 mg protein equivalent in 3 mL of alkaline saline (pH 8.0) were incubated with 250 µg of ICG dye by incubating in a shaker with 100 rpm for 6 h. The samples were diluted to 13 mL using physiological saline and ultracentrifuged at 100 000 × *g* for 2 h to remove the unconjugated free ICG. The pellet was resuspended in 1.5 mL of physiological saline and used for the quantification of conjugated ICG using optical fluorescence imaging. The samples diluted in different protein equivalents (0.3125–10 µg) were fluorescently imaged along with ICG standard (0.625–10 µg) using an IVIS optical imaging system in the ICG fluorescent window (Ex-710/Em-830nm). The conjugated ICG in protein equivalent was estimated using the formula generated from the standard graph. The conjugation efficiency of ICG to EV protein was also

evaluated by resolving the proteins in 4–12% gradient SDA PAGE using optical fluorescence imaging.

Proteomic Analysis: Proteomic analysis was performed by using a method reported previously.[28] In brief, the protein samples collected from 4T1-eEVs were digested overnight at 37 °C following the addition of 1 µg trypsin per 20 µg of protein, and we reconstituted the tryptic peptide samples in 15 µL of 0.1% formic acid in water. The authors injected ≈10 µg (8 µL samples) of protein from each sample onto a C18 PepMap100 trap column using an UltiMate Rapid Separation Liquid Chromatography System (Dionex) with a flow rate of 5 µL min^{-1} using 0.1% formic acid in water as a running solution. Peptides were then separated by reversed-phase chromatography on a 25 cm long C18 analytical column packed in-house with Magic C18AQ (Michrom Bioresources). A multistep gradient protocol was used to elute peptides from the column, and these eluted peptides were used for LC-MS/MS analysis using an LTQ-Velos Orbitrap mass spectrometer (Thermo Fisher Scientific).

Investigation on the Targeting and Functional Effect of 4T1-eEVs-PNCs: The authors seeded 4T1 cells at a density of 5×10^3 cells $well^{-1}$ in 96-well plates and after 24 h the cells were transfected with two different concentrations of uPAR siRNA or nonspecific siRNA (Santa Cruz Biotechnology, Santa Cruz, CA) using Lipofectamine 2000 (Invitrogen) according to the manufacturer's instructions. After uPAR-siRNA treatment, the eEVs-(ScuPA) PLGA-antimiRNA-21-Cy5 or eEVs-(uPA) PLGA-antimiRNA-21-Cy5 (1×10^7 EVs $well^{-1}$) was added to the cell culture and acquired fluorescence imaging using Celigo, as described previously.[33] To investigate the chemosensitizing functional effect of 4T1-eEVs-PNCs, the authors seeded the 4T1 cells at a density of 1×10^5 cells $well^{-1}$ in 12-well plates. The authors then treated the cells with eEV-NPs (5×10^7 EVs $well^{-1}$) for 24 h and treated them with doxorubicin 0.5 µM for a further 48 h. The synergistic cytotoxicity effect of 4T1-eEVs-PNCs was investigated independently loaded with either antisense miRNAs-21 or antisense miRNAs-10b + DOX cells using the Cell titer blue (CTB) assay, as described previously with minor modifications.[34]

Investigation of TNBC Tumor-Targeting Ability of 4T1-eEVs-PNCs in Syngeneic 4T1 Tumor-Bearing Nude Mouse Model: The authors purchased 6-week-old nude mice (nu nu^{-1}), weighing 15–20 g, from Charles River Laboratories (Wilmington, MA, USA) and we housed them in an environment with a controlled temperature (22 °C), humidity, and a 12 h light/dark cycle. All the animal experiments were conducted according to a protocol approved by our University Institutional Animal Care and Use Committee guidelines and in adherence to the NIH Guide for the Care and Use of Laboratory Animals (26308). The tumor-bearing nude mouse models were prepared by subcutaneous injection of 0.1 mL 4T1 cell suspension (1×10^6 cells) into the right and left mouse flanks. To visualize the 4T1-eEV-PNCs, the eEVs were labeled with indocyanine green (ICG) and then fused with different 4T1-eEV-PNCs nanoformulations as reported previously.[26,33] For in vivo biodistribution, tumor-bearing mice were randomly assigned to two experimental groups, with five mice per group. The nanococktail mixture of ICG-labeled Sc-uPA or uPA-4T1-eEVs-PNCs independently loaded with either antisense miRNAs-21 or antisense miRNAs-10b (150 µL, $3–4 \times 10^{11}$ NPs; ≈90 µg protein equivalent with ≈14.4 µg of conjugated ICG dye) were injected via the tail vein. The whole-body biodistribution at various time points with excitation and emission wavelengths of 745 nm and 820 nm, respectively, were recorded using the Lago-X optical imaging instrument (from Spectral Instruments, LLS, Tucson, AZ). Mice in the DOX treatment group received 5 mg kg^{-1} DOX in 100 µL saline with 10% PEG-400 by intraperitoneal injection. At study termination, mice were euthanized by CO_2 asphyxiation, and the liver, spleen, kidneys, heart, lungs, and tumors were excised and immediately imaged. The emitted fluorescence was quantified using Aura Image analysis software over the region of interest (ROI). To further investigate the tumor accumulation of 4T1-eEVs-PNCs, a hemispherical Photoacoustic (PAI) imaging system (Nexus 128 scanner, Endra Inc., Ann Arbor, MI) was used as described previously.[33,35]

Investigation of the TNBC-Targeted Combinational Antitumor Effects of 4T1-eEVs-PNCs in the Syngeneic 4T1 Tumor-Bearing Immunocompetent Mouse Model: An immunogenic mouse breast cancer cell line, 4T1, was used to establish the tumor model in syngeneic immunocompetent BALB/c mice, as described previously.[26,36] All animal procedures were approved by the Institutional Administrative Panel on Laboratory Animal Care. The authors subcutaneously injected 4T1 cells (1.0×10^6 cells in 50 µL PBS) mixed with 50 µL of Matrigel in the right and left mouse flanks and allowed these to grow to a tumor size ≈0.1 cm^3, at which point we measured tumor volumes; thereafter, tumors were routinely measured twice a week until the experiments were completed. Metastasis to the lungs in 4T1 tumor-bearing mice was detected from Day 18 onward; liver metastasis was also observed at a later stage. Tumor volumes were calculated in mm^3 using the following formula: $(L \times W \times H)/2$, where L is the length, W is the width, and H is the height); alternatively, the method (L x W^2)/2 was used when the width and height of the tumors were equal.

Ex Vivo Histology and RT-PCR Analysis: The ex vivo histology and RT-PCR quantification were performed for the delivered antisense microRNAs by following the protocols published previously by the authors.[24,26,37]

Statistical Analyses: All statistical analyses were performed using Student's *t* test and Prism software (Version 8.4.1, GraphPad, LLC). The results were presented as mean ± standard deviation (SD). All statistical tests were two-tailed, unless otherwise stated. The results were considered to be statistically significant when the corresponding *p*-value was <0.05.

Supporting Information

Supporting Information is available from the Wiley Online Library or from the author.

Acknowledgements

The authors would like to thank the Canary Center at Stanford, Department of Radiology for providing the facility and resources for this research. The authors would also like to thank Stanford Animal Histology Services for the preparation of histology slides and histological analysis of animal tissues. The authors thank the Small Animal Imaging Facility at Stanford Center for Innovation in in vivo Imaging and Dr. Frezghi Habte for his technical support in performing ultrasound, photoacoustic imaging, and confocal microscopy. The authors also thank Elise Robinson for her technical assistance in performing NTA analysis. This work was in part supported by the Focused Ultrasound Foundation and the National Institutes of Health (Grant numbers R01CA209888 and R21EB022298). NIH S10OD023518-01A1 Award for the Celigo S Imaging Cytometer (200-BFFL-S) to R.P. is acknowledged. Gary Glazer-GE Gift Fund (Department of Radiology, Stanford University).

Conflict of Interest

The authors declare no conflict of interest.

Author Contributions

R.P. and R.J.C.B. conceived the idea and designed the experiments for this study; R.J.C.B., Y.Z., F.J.G., U.K.S., F.H., and R.P. carried out the experiments and were involved in data acquisition and analysis. R.J.C.B., J.M., S.P., T.F.M., and R.P. wrote and edited the manuscript.

Data Availability Statement

The data that support the findings of this study are available from the corresponding author upon reasonable request.

Keywords

antisense miRNA, cell free cancer therapeutics, engineered nanococktails, targeted combinational cancer therapy, triple-negative breast cancer

Received: July 12, 2021
Revised: November 28, 2021
Published online: December 17, 2021

[1] H. Sung, J. Ferlay, R. L. Siegel, M. Laversanne, I. Soerjomataram, A. Jemal, F. Bray, *CA Cancer J. Clin.* **2021**, *71*, 209.
[2] a) M. Brown, A. Tsodikov, K. R. Bauer, C. A. Parise, V. Caggiano, *Cancer* **2008**, *112*, 737; b) A. Marra, D. Trapani, G. Viale, C. Criscitiello, G. Curigliano, *npj Breast Cancer* **2020**, *6*, 1.
[3] L. Malorni, P. Shetty, C. De Angelis, S. Hilsenbeck, M. Rimawi, R. Elledge, C. Osborne, S. De Placido, G. Arpino, *Breast Cancer Res. Treat.* **2012**, *136*, 795.
[4] A. Möller, R. J. Lobb, *Nat. Rev. Cancer* **2020**, *20*, 1.
[5] C. Y. Goh, C. Wyse, M. Ho, E. O'Beirne, J. Howard, S. Lindsay, P. Kelly, M. Higgins, A. McCann, *Cancer Lett.* **2020**, *473*, 90.
[6] T. J. Smyth, J. S. Redzic, M. W. Graner, T. J. Anchordoquy, *Biochimica et Biophysica Acta (BBA)-Biomembranes* **2014**, *1838*, 2954.
[7] a) H. Sun, S. Burrola, J. Wu, W.-Q. Ding, *Int. J. Mol. Sci.* **2020**, *21*, 6097; b) M. Guo, F. Wu, G. Hu, L. Chen, J. Xu, P. Xu, X. Wang, Y. Li, S. Liu, S. Zhang, *Sci. Transl. Med.* **2019**, *11*.
[8] a) K. Dooley, R. E. McConnell, K. Xu, N. D. Lewis, S. Haupt, M. R. Youniss, S. Martin, C. L. Sia, C. McCoy, R. J. Moniz, *Mol. Ther.* **2021**, *29*, 1729; b) H. Kim, D. Kim, H. Nam, S. Moon, Y. J. Kwon, J. B. Lee, *Methods* **2019**, *177*, 80.
[9] Z. Ye, T. Zhang, W. He, H. Jin, C. Liu, Z. Yang, J. Ren, *ACS Appl. Mater. Interfaces* **2018**, *10*, 12341.
[10] P. Scodeller, E. K. Asciutto, *Molecules* **2020**, *25*, 808.
[11] M. C. Huber, R. Mall, H. Braselmann, A. Feuchtinger, S. Molatore, K. Lindner, A. Walch, E. Gross, M. Schmitt, N. Falkenberg, *BMC Cancer* **2016**, *16*, 615.
[12] a) Y. Liang, L. Duan, J. Lu, J. Xia, *Theranostics* **2021**, *11*, 3183; b) L. Alvarez-Erviti, Y. Seow, H. Yin, C. Betts, S. Lakhal, M. J. Wood, *Nat. Biotechnol.* **2011**, *29*, 341.
[13] J. M. Miller-Kleinhenz, E. N. Bozeman, L. Yang, *Wiley Interdiscip. Rev.: Nanomed. Nanobiotechnol.* **2015**, *7*, 797.
[14] a) N. Mahmood, C. Mihalcioiu, S. A. Rabbani, *Front. Oncol.* **2018**, *8*, 24; b) J. Madunić, *Thromb. Haemostasis* **2018**, *118*, 2020.
[15] A. Thielemann, A. Baszczuk, P. Kopczyński, Z. Kopczyński, *Contemp. Oncol.* **2013**, *17*, 440.
[16] M. Jo, B. M. Eastman, D. L. Webb, K. Stoletov, R. Klemke, S. L. Gonias, *Cancer Res.* **2010**, *70*, 8948.
[17] R. Devulapally, N. M. Sekar, T. V. Sekar, K. Foygel, T. F. Massoud, J. r. K. Willmann, R. Paulmurugan, *ACS Nano* **2015**, *9*, 2290.
[18] a) L. Yang, Z. Cao, H. K. Sajja, H. Mao, L. Wang, H. Geng, H. Xu, T. Jiang, W. C. Wood, S. Nie, *J. Biomed. Nanotechnol.* **2008**, *4*, 439; b) L. Hansen, E. K. U. Larsen, E. H. Nielsen, F. Iversen, Z. Liu, K. Thomsen, M. Pedersen, T. Skrydstrup, N. C. Nielsen, M. Ploug, *Nanoscale* **2013**, *5*, 8192; c) M. Wang, A. D. Miller, M. Thanou, *J. Drug Targeting* **2013**, *21*, 684.
[19] L. Ma, J. Teruya-Feldstein, R. A. Weinberg, *Nature* **2007**, *449*, 682.
[20] S. Khalighfard, A. M. Alizadeh, S. Irani, R. Omranipour, *Sci. Rep.* **2018**, *8*, 17981.
[21] R. Rupaimoole, F. J. Slack, *Nat. Rev. Drug Discovery* **2017**, *16*, 203.
[22] A. V. Telichko, H. Wang, S. Bachawal, S. U. Kumar, J. C. Bose, R. Paulmurugan, J. J. Dahl, *Ultrasound Med. Biol.* **2020**, *47*, 309.
[23] T. Di Ianni, R. J. Bose, U. K. Sukumar, S. Bachawal, H. Wang, A. Telichko, C. Herickhoff, E. Robinson, S. Baker, J. G. Vilches-Moure, *J. Controlled Release* **2019**, *309*, 1.
[24] S. U. Kumar, A. V. Telichko, H. Wang, D. Hyun, E. G. Johnson, M. S. Kent, R. B. Rebhun, J. J. Dahl, W. T. Culp, R. Paulmurugan, *Adv. Ther.* **2020**, *3*, 2000120.
[25] a) T.-Y. Wang, J. W. Choe, K. Pu, R. Devulapally, S. Bachawal, S. Machtaler, S. M. Chowdhury, R. Luong, L. Tian, B. Khuri-Yakub, *J. Controlled Release* **2015**, *203*, 99; b) R. Devulapally, T. V. Sekar, R. Paulmurugan, *Mol. Pharmaceutics* **2015**, *12*, 2080.
[26] R. JC Bose, S. Uday Kumar, Y. Zeng, R. Afjei, E. Robinson, K. Lau, A. Bermudez, F. Habte, S. J. Pitteri, R. Sinclair, *ACS Nano* **2018**, *12*, 10817.
[27] M. Kanada, B. D. Kim, J. W. Hardy, J. A. Ronald, M. H. Bachmann, M. P. Bernard, G. I. Perez, A. A. Zarea, T. J. Ge, A. Withrow, S. A. Ibrahim, V. Toomajian, S. S. Gambhir, R. Paulmurugan, C. H. Contag, *Mol. Cancer Ther.* **2019**, *18*, 2331.
[28] R. J. C. Bose, N. Tharmalingam, F. J. Garcia Marques, U. K. Sukumar, A. Natarajan, Y. Zeng, E. Robinson, A. Bermudez, E. Chang, F. Habte, S. J. Pitteri, J. R. McCarthy, S. S. Gambhir, T. F. Massoud, E. Mylonakis, R. Paulmurugan, *ACS Nano* **2020**, *14*, 5818.
[29] R. J. Bose, B. J. Kim, Y. Arai, I.-b. Han, J. J. Moon, R. Paulmurugan, H. Park, S.-H. Lee, *Biomaterials* **2018**, *185*, 360.
[30] a) R. J. Bose, S.-H. Lee, H. Park, *Drug Discovery Today* **2016**, *21*, 1303; b) R. J. Bose, R. Paulmurugan, J. Moon, S.-H. Lee, H. Park, *Drug Discovery Today* **2018**, *23*, 891.
[31] A. Hoshino, B. Costa-Silva, T.-L. Shen, G. Rodrigues, A. Hashimoto, M. T. Mark, H. Molina, S. Kohsaka, A. Di Giannatale, S. Ceder, *Nature* **2015**, *527*, 329.
[32] M. Kanada, M. H. Bachmann, J. W. Hardy, D. O. Frimannson, L. Bronsart, A. Wang, M. D. Sylvester, T. L. Schmidt, R. L. Kaspar, M. J. Butte, *Proc. Natl. Acad. Sci. U. S. A.* **2015**, *112*, E1433.
[33] R. J. Bose, N. Tharmalingam, F. J. Garcia Marques, U. K. Sukumar, A. Natarajan, Y. Zeng, E. Robinson, A. Bermudez, E. Chang, F. Habte, *ACS Nano* **2020**, *14*, 5818.
[34] N. Kumar, R. Afjei, T. F. Massoud, R. Paulmurugan, *Sci. Rep.* **2018**, *8*, 16363.
[35] D. Van de Sompel, L. S. Sasportas, A. Dragulescu-Andrasi, S. Bohndiek, S. S. Gambhir, *PLoS One* **2012**, *7*, e45337.
[36] F. Zheng, P. Li, S. V. Bachawal, H. Wang, C. Li, W. Yuan, B. Huang, R. Paulmurugan, *Mol. Imaging Biol.* **2020**, *22*, 1003.
[37] H. Wang, Z. Hu, U. K. Sukumar, R. J. C. Bose, A. Telichko, J. J. Dahl, R. Paulmurugan, *Nanotheranostics* **2022**, *6*, 62.